Nano Research
2023, 16(5): 6593–6600

ISSN 1998-0124 CN 11-5974/O4
https://doi.org/10.1007/s12274-023-5381-z

Research Article

Fabrication of N,S co-doped carbon immobilized high-density Co single atoms toward electro-oxidation of organic sulfides with water as feedstock

Pei Zhu[1,§], Wen-Xiong Shi[1,§], Ying Wang[3], Zhi-Ming Zhang[1] (✉), Lina Li[2] (✉), and Changhua An[1] (✉)

[1] *Tianjin Key Laboratory of Organic Solar Cells and Photochemical Conversion, Tianjin Key Laboratory of Advanced Functional Porous Materials, Institute for New Energy Materials & Low-Carbon Technologies, Tianjin University of Technology, Tianjin 300384, China*
[2] *Shanghai Synchrotron Radiation Facility, Shanghai Advanced Research Institute, Chinese Academy of Sciences, Shanghai 201204, China*
[3] *Department of Chemistry, The Chinese University of Hong Kong, Shatin, New Territories, Hong Kong 999077, China*
[§] *Pei Zhu and Wen-Xiong Shi contributed equally to this work.*

Received: 19 September 2022 / **Revised:** 29 November 2022 / **Accepted:** 4 December 2022

ABSTRACT

Development of high-density single atoms site (SAs) electrocatalysts is highly desirable due to their extraordinary catalytic performance. However, their synthesis is still challenging and their anticorrosion capacities in electrolyte (particularly in acidic electrolyte) are unsatisfying. Herein, we have constructed N,S co-doped carbon to anchor ~ 10 wt.% Co SAs (Co-SAs/NSC) via a novel polymerization–sulfurization–pyrolysis strategy toward selective electro-oxidation of thioethers in acidic solution. The as-obtained Co SAs has a coordination geometry of Co-S_2N_4, exhibiting excellent electrocatalytic activity and robust stability. At a low potential of 1.40 V vs. reversible hydrogen electrode (RHE), the conversion rate of thioethers over Co-SAs/NSC reaches 99.7% with 100% selectivity and 100% Faraday efficiency (FE) for producing sulfoxide, which is higher than the commercial Pt electrode and the reported state-of-the-art catalysts. Theoretical calculations and experiments reveal that the Co-S_2N_4 structure endows the outstanding electro-oxidation activity of Co SAs through significantly promoting desorption of the products. This work presents a convenient strategy to build high-performance SAs catalysts for the resourceful use of sulfur-containing pollutants.

KEYWORDS

single-atom, cobalt, high density, selective oxidation, electrocatalysis

1 Introduction

Carbon supported single atom site (SAs) catalysts with exceptional electrocatalytic performance suffer from either low loadings (< 5 wt.%) or complex manufacturing processes [1–10]. Nitrogen-doped carbon has been used as a robust support to immobilize various isolated metal SAs through the interaction of metal–N bond [1–10]. Nevertheless, the single N-staibilized SAs often experience insufficient durability and decayed catalytic activities, particularly in response to electrocatalytic oxidation reation in acidic electrolyte. Recent advances demonstrate the S-embedded nitrogen-doped carbon can effectively ameliorate the anticorrosion capacity and maintain the initial activity on the catalysts [11, 12]. Especially, the formed metal–S bond can increase the loading of SAs up to above 7 wt.% through enhancing the interaction with support [13]. However, it is still lower than the expected values for the preparation of high loading metal SAs on carbon. Therefore, the achievement of as much as SAs still remains a great challenge, which hampers the progress on accelerating their practical applications to some extent.

Transition-metal nanocatalysts represent a class of excellent electrocatalysts toward selective oxidation of cost-effective organics (e.g., alcohols, aldehydes, amines, and biomass) to value-added chemicals [14–19]. However, for the electro-oxidaiton conversion of thioethers, which are ubiquitous pollutants in processing fuels, the existing electrocatalysts generally are universially inert at low working voltage, and the gaseous O_2 is also required during the reactions [20–22]. While the selective oxidation products of sulfoxides and sulfones are important chemicals for pharmaceuticals, functional materials, and organic catalysts [23, 24]. Thus, it is highly desirable to design and explore efficient electrocatalysts toward the achievement of presional conversion of thioethers. In view of the ultra-high performance of SAs, SAs catalysts can be expected to be a class of excellent candidates for electro-oxidation of thioethers. Particularly, the SAs featuring clear coordination configuration are in favor of identifying the underlying reaction mechanisms and deciphering the structure–performance relationship at the atomic level. As far as we know, utilizing metal SAs to implement the efficient electro-oxidation of thioethers has not been reported.

Herein, we developed a novel polymerization–sulfurization strategy to fabricate N,S co-doped commercial carbon (NSC) loading ~ 10 wt.% Co SA (Co-SAs/NSC). The dual-atoms doped carbon endows the Co-SAs/NSC with a unique Co-S_2N_4 geometry structure, delivering high performance and robust stability for electro-oxidation of various thioethers. Taking electro-oxidation of methyl phenyl sulfide (MPS) as an example, the conversion of

Address correspondence to Zhi-Ming Zhang, zmzhang@email.tjut.edu.cn; Lina Li, lilina@sinap.ac.an; Changhua An, anchua@ustc.edu

MPS over Co-SAs/NSC reaches a rate of 99.7% with 100% selectivity for methylphenyl sulfoxide (MPSO) and 100% Faraday efficiency (FE) at a low voltage of 1.40 V vs. reversible hydrogen electrode (RHE). The performance is much superior to that of commercial Pt electrode and state-of-the-art catalysts. A series of experimental analysis shows that the active [O] species originate from water. Furthermore, density functional theory (DFT) calculation further reveals that the unique structure of Co-S_2N_4 significantly promotes desorption of products.

2 Experimental

2.1 Chemicals

Commercial carbon black (C, 99.9%, Alfa), pyrrole (py, C_4H_5N, 99%, Macklin), thiourea (H_4CN_2S, AR, Sinopharm), 2,2-bipyridine ($C_{10}H_8N_2$, 99%, Macklin), ammonium persulfate ($H_8N_2O_8S_2$, 98%, Aladdin), cobalt chloride hexahydrate ($CoCl_2{\cdot}6H_2O$, AR, Macklin), ethanol (C_2H_6O, > 99.7%, Aladdin), potassium sulfate (K_2SO_4, AR, Macklin), and glacial acetic acid ($C_2H_4O_2$, AR, Macklin) were purchased and used as received without further purification. The ultrapure distilled water (DIW, 18.25 MΩ) was applied in all the experiments.

2.2 Preparation of NSC

NSC support was prepared via thermal treatment of thiourea and polypyrrole (Ppy) coated commercial carbon. Briefly, commercial carbon (0.5 g) was dispersed into ethanol/water solution (60 mL, v/v = 1:5) with vigorous stirring for 0.5 h. 500 μL of fresh pyrrole was introduced dropwise into the above dispersion and stirred 4 h in darkness. $(NH_4)_2S_2O_8$ solution (15 mL, 200 mg) was then slowly injected into the suspension and continuously stirred 12 h to initiate the polymerization of py. Subsequently, dialysis was performed to remove the residual reagents. Ppy coated carbon was collected by freeze-drying, the pyrolysis of which together with thiourea (1:10, mass ratio) under NH_3 atmosphere at 700 °C for 3 h resulted in the formation of NSC support.

2.3 Preparation of Co-SAs/NSC

The Co-SAs/NSC was prepared by thermal decomposition of cobalt-complex ($[Co(bipy)_n]^{2+}$) on the surface of NSC. Briefly, 30 mg of NSC was dispersed into ethanol/water solution (15 mL, v/v = 1:2) and vigorously stirred 4 h. After the $CoCl_2{\cdot}6H_2O$ (13.3 mg) and 2,2-bipyridine (bipy, 17.5 mg) were dissolved in ethanol and water solution (10 mL, v/v = 1:1), the mixture was dripped into NSC suspension and stirred 5 h at room temperature. After being collected by freeze-drying, the obtained solid mixture was pyrolyzed at 300 °C for 2 h under 10% H_2/Ar atmosphere. The loading of Co atoms was determined to be ca. 10 wt.% by inductively coupled plasma-mass spectrometry (ICP-MS). For comparison, elevating the pyrolysis temperature to 350 °C led to the formation of Co-based nanopartiles (Co-NPs)/NSC.

2.4 Characterizations

The morphologies of the samples were observed on scanning electron microscopy (SEM) (Hitachi S-4800) and transmission electron microscopy (TEM) (TECNAI G2 Spirit TWIN). High resolution TEM (HRTEM) was done with a JEM-2100F equipped with energy-dispersive X-ray spectroscopy (EDS). Aberration-corrected high angle annular dark-field scanning transmission electron microscopy (HAADF-STEM) images of atomic dispersion of Co were examined by FEI-Titan Cubed Themis G2 300. X-ray diffraction (XRD) was recorded with a Rigaku Corporation UItimaIV diffractometer using a Cu Kα source (λ = 0.15406 nm). Raman spectra were conducted on a Renishaw-200 visual Raman microscope with a laser beam of 633 nm. The adsorption isotherms of nitrogen were measured by using automatic volumetric adsorption equipment (BELSORP mini II, BEL), and the surface areas were calculated using N_2 sorption data at 77 K. X-ray photoelectron spectroscopy (XPS) was recorded on a scanning X-ray microprobe (PHI 5000 Verasa, ULAC-PHI, Inc.). Thermogravimetric analysis (TGA) was obtained on Netzsch (TG 209 F3, Germany) with a heating rate of 10 °C·min^{-1} under N_2 atmosphere. The content of Co was determined by ICP-MS (iCAP RQ, Germany). High performance liquid chromatography (HPLC) was measured on Shimadzu ultraviolet–visible detector of 254 nm using a 4.6 mm × 150 mm Shim-pack GWS 5 μm C18 column. The gas chromatography (GC) was recorded on FuLi 9790II with thermal conductivity detector (TCD) and flame ionization detector (FID). The injection temperature was set at 120 °C and N_2 was used as the carrier gas at 1.0 mL·min^{-1}.

2.5 Electrocatalytic performance evaluation

The electro-oxidation was performed in a divided H-type three-compartment electrochemical cell at room temperature, consisting of a working electrode, counter electrode of graphite rod, and reference saturated SCE electrode, respectively. Linear sweep voltammetry (LSV) with the scan rate of 10 mV·s^{-1} and chronoamperometry (*i*–*t*) tests were performed in the mixture of 0.5 M CH_3COOH and 0.25 M K_2SO_4 (pH = ca. 2.8) on an electrochemical workstation (CHI 660E, Shanghai Chenhua). All the potentials were referred to the RHE by following equation ($E_{RHE} = E_{SCE} + 0.241 + 0.059$ pH).

The working electrode was prepared as follows. The as-synthesized catalyst (5 mg) was dispersed in an ethanol/Nafion solution (500 μL, v/v = 9:1) under sonicating 30 min. Subsequently, the catalyst (ca. 0.5 mg) was dripped onto a piece of carbon cloth (1 cm × 1 cm). The electro-oxidation of MPS was conducted in the above electrolyte solution (30 mL) containing 0.5 mmol MPS. The stability tests of the catalyst were investigated by *i*–*t* at 1.40 V vs. RHE. The electrochemical double-layer capacitance (C_{dl}) was determined by cyclic voltammograms (CV) measured at a potential region of 0.55–0.65 V vs. RHE with scanning rates from 10 to 100 mV·s^{-1}. The electrochemical active surface area (ECSA) was yielded based on the equation of ECSA = geometric area of working electrode × $C_{dl}/C_{dl\ ref}$, where $C_{dl\ ref}$ as roughness factor is typically assumed to be 40 μF·cm^{-2}.

2.6 Synchronic X-ray absorption fine structure (XAFS)

The XAFS data (Co K-edge) were collected at BL14W1beamline on the Shanghai Synchrotron Radiation Facility (SSRF) with a transmission mode. ATHENA module of Demeter software packages was used to process the acquired data and the ARTEMIS module of Demeter software packages was used for least-squares curve fitting. The amplitude reduction factor (S_0^2) was obtained via model sample fitting and was fixed in the subsequent fitting for Co-SA/NSC, while the internal atomic distances *R*, DebyeWaller factor σ^2, and the edge-energy shift ΔE_0 were set to run freely. The extended X-ray absorption fine structure (EXAFS) spectrum fitting was conducted under the boundary conditions with *k*-space ranging from 2.45 to 10.25 Å^{-1}, and *R*-space ranging from 1 to 3.2 Å^{-1}.

2.7 Computation method

All the energy calculations have been performed based on DFT by CASTEP code [25–27]. The Co single atoms was put into the two graphene layers and the S_2–Co–N_4 bond length was frozen, which is determined by experimental results. After geometry optimization, the stable structure of Co atom with two graphene

layers was obtained. Then, the MPS molecules were put on the Co single atoms and nanoparticles, respectively. The geometry optimization calculations were performed with the positions of single atom Co, and Co nanoparticles were frozen with the fixed sizes of cell length (with box length 16 angstrom). The Perdew–Burke–Ernzerhof (PBE) function within the generalized gradient approximation (GGA) method [27] and Broyden–Fletcher–Goldfarb–Shanno update scheme [28] were utilized to explore the optimizing structure with a minimum energy. The ultrasoft pseudopotential formalism was applied in our simulation system and the energy cut off of electron wave function was set as 380 eV [29]. The *k*-points were set as 4 × 4 × 1 grid in reciprocal space so as to save computation source. The convergence tolerance was set to 5×10^{-7} eV for energy variation. Finally, the free energies of each system were calculated to estimate the energy difference in the catalyst process.

3 Results and discussion

3.1 Synthesis and characterization of Co-SAs/NSC

Figure 1(a) illustrates a typical process for the synthesis of Co-SAs/NSC. Briefly, the carbon-based polymer was firstly prepared via the polymerization of py with commercial carbon as template and ammonium persulfate as oxidant, respectively. Then the NSC was fabricated by co-pyrolysis of the polymer and thiourea under NH_3 atmosphere at 700 °C for 3 h. XPS analysis shows abundant N and S atoms are on the surface of NSC (Table S1 in the Electronic Supplementary Material (ESM)). Meanwhile, the Co source was also pre-treated by coordination of Co^{2+} ions and bipy to form complex of $[Co(bipy)_n]^{2+}$ with porphyrin-like structure (Fig. S1 in the ESM). The Co-complex can be uniformly adsorbed on the NSC by π–π conjugation. Finally, the pyrolysis of the obtained precursors resulted in the formaiton of Co-SAs/NSC under H_2/Ar atmosphere at 300 °C for 2 h according to the TGA result (Fig. S2 in the ESM). The Co content is determined to be ca. 10 wt.% by ICP-MS.

SEM image shows the as-synthesized Co-SAs/NSC consists of ultrafine nanospheres with rough surface (Fig. 1(b) and Fig. S3 in the ESM). TEM and HRTEM images indicate no Co nanoparticles or nanoclusters in Co-SAs/NSC (Figs. 1(c) and 1(d), and Fig. S4 in the ESM), which is in agreement with the XRD pattern (Fig. S5 in the ESM). HAADF-STEM image with sub-angstrom resolution clearly shows dense and isolated Co SAs were distributed on the NSC (Fig. 1(d)). EDS mapping demonstrates the presence of elemental Co, C, N, and S in the obtained sample and the uniform distribution of Co sites over the whole architecture (Fig. 1(f)). Raman spectra of Co-SAs/NSC, as given in Fig. S6 in the ESM, reveal the D band (1340 cm^{-1}) and G band (1570 cm^{-1}) for the disordered carbon or defective graphitic structure, and the characteristic peak of graphitic layers, respectively [30]. Their intensity ratio (I_D/I_G = 1.15) suggests the abundant defects in NSC [31]. Furthermore, the surface porous feature of Co-SAs/NSC was investigated by N_2 adsorption–desorption isotherms (Fig. S7 in the ESM), in which the specific surface area and average pore diameter are determined to be ca. 68.9 $m^2 \cdot g^{-1}$ and ca. 2.5 nm, respectively.

To gain the detailed structural information of Co SAs, the X-ray absorption near edge structure (XANES) and EXAFS were performed on the Co-SAs/NSC. As shown in Fig. 2(a), XANES of Co K-edge reveals the white line intensity of Co-SAs/NSC is between those of Co foil and Co_3O_4, implying that the Co atoms are in a positive oxidation state. The semi-quantitative analysis shows the average valance of Co is roughly +1.64 (Fig. S8 in the ESM) [32]. The Fourier transform EXAFS in *R* space exhibits one prominent peak at ca. 1.67 Å (Fig. 2(b)), which can be assigned to the scattering of Co–N and Co–S. The structure is different from the reported Co SAs [33–37]. Obviously, the characteristic Co–Co bond of Co foil (ca. 2.16 Å) cannot be observed, further

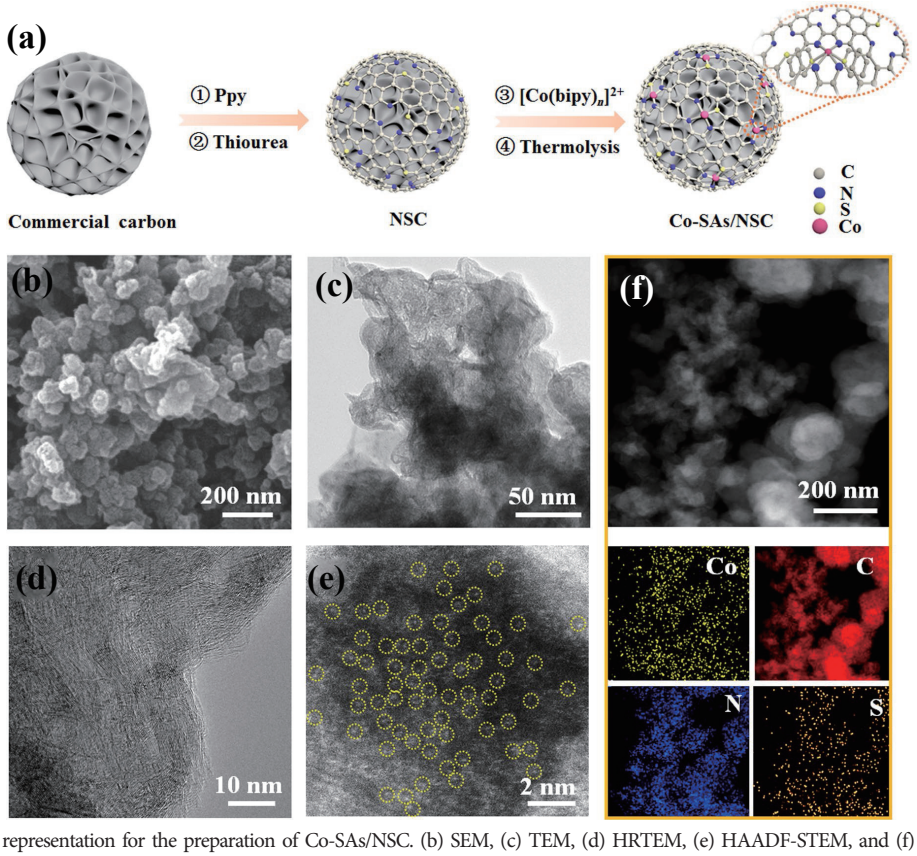

Figure 1 (a) Schematic representation for the preparation of Co-SAs/NSC. (b) SEM, (c) TEM, (d) HRTEM, (e) HAADF-STEM, and (f) elemental EDS-mapping images of the as-obtained Co-SAs/NSC. Isolated highlighting spots in (e) represent the Co SAs in the sample.

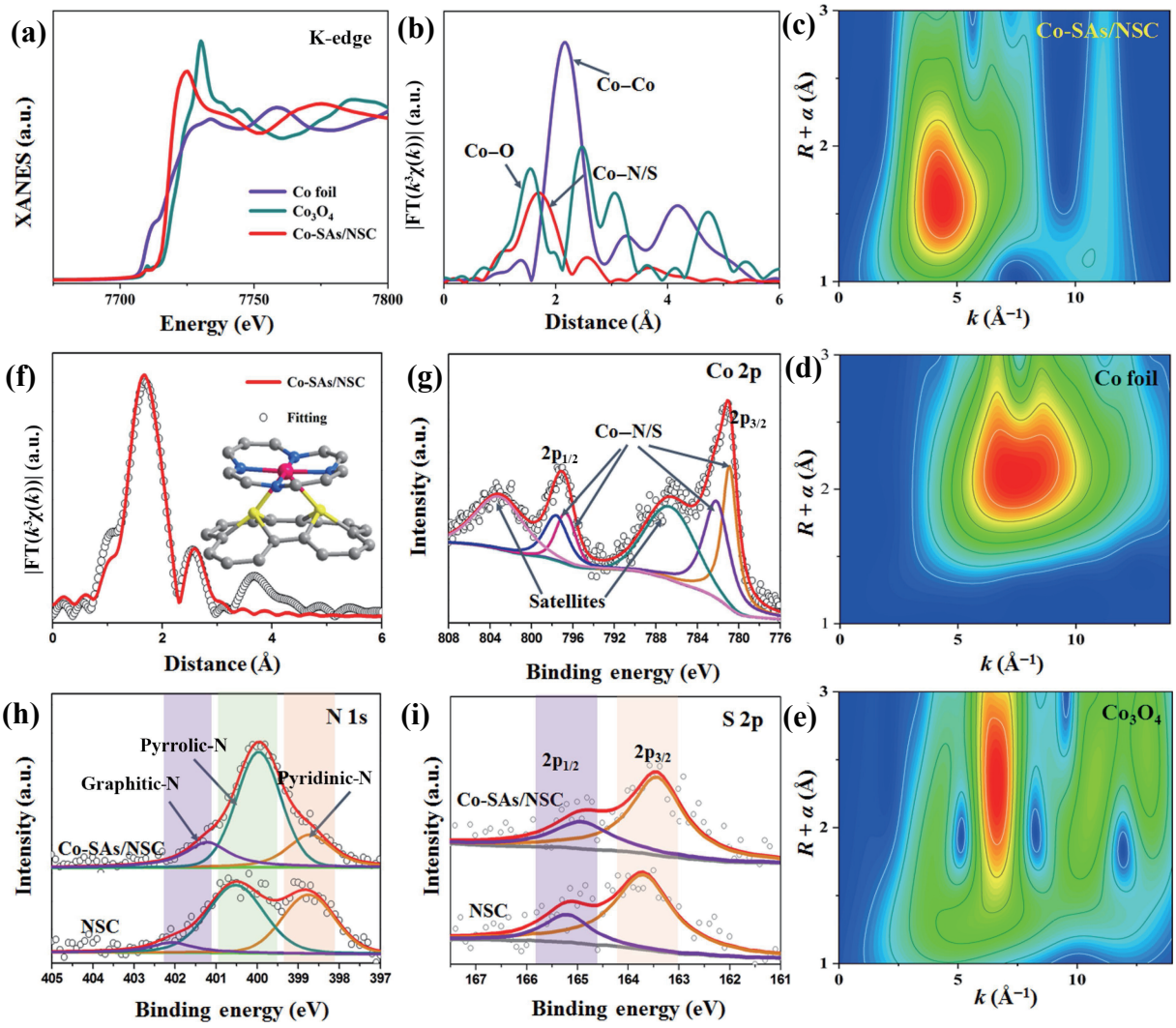

Figure 2 (a) XANES spectra of Co K-edge in Co-SAs/NSC, Co foil, and Co_3O_4. (b) Fourier transformation (FT) of k^3-weighted EXAFS spectra of Co-SAs/NSC, Co foil, and Co_3O_4. WT for the k^3-weighted EXAFS signals of (c) Co-SAs/NSC, (d) Co foil, and (e) Co_3O_4. (f) EXAFS fitting curves of Co-SAs/NSC at *R* space. High resolution XPS spectra of (g) Co 2p, (h) N 1s, and (i) S 2p for Co-SAs/NSC.

demonstrating the individual distribution of Co atoms on the NSC, which is consistent with the HAADF-STEM. The EXAFS wavelet transform (WT) analysis concurrently gives the radial distance resolution and *k*-space resolution, which can be employed to investigate the coordination environment of the Co atoms. Figure 2(c) shows the maximal WT intensity with the light atom coordination at 1.67 Å in Co-SAs/NSC switching to ca. 4.4 $Å^{-1}$, which is different from Co foil (7.6 $Å^{-1}$) and Co_3O_4 (6.6 $Å^{-1}$, Figs. 2(d) and 2(e)). These results further demonstrate that Co atom is monoatomic state and substantiates the assignment of the major peak at ~ 1.67 Å to Co–N/S bonding. Quantitative space spectra fitting further confirm the Co atom was in a Co-S_2N_4 mode on the first coordination shell (Fig. 2(f), and Fig. S9 and Table S3 in the ESM).

XPS was performed to further study the surface electronic structure of Co-SAs/NSC. As illustrated in Fig. 2(g), the binding energy peaks at 780.9 and 782.15 eV can be assigned to Co $2p_{3/2}$ for Co–N/Co–S bond [13, 33], which is in agreement with XANES. The N 1s high-resolution XPS spectrum demonstrates the existance of pyridinic-N (398.7 eV), pyrrolic-N (399.9 eV), and graphitic-N (401.2 eV) in the sample, respectively (Fig. 2(h)) [38]. Specifically, these peaks related to pyrrolic-N and graphitic-N species evidently shift towards lower binding energy after immobilizing Co SAs. Similar phenomenon was also observed in the S 2p high-resolution XPS spectrum (Fig. 2(i)), implying the electrons transfer (interaction) between Co atoms and N, S atoms [39]. The C 1s high-resolution XPS spectrum is deconvoluted into three types of carbon signals (Fig. S10 in the ESM), corresponding to C–C (284.7 eV), C–N (285.6 eV), and C–S (286.8 eV), respectively.

In view of Co SAs with unique coordination structure of Co-S_2N_4, the N, S heteroatoms are pivotal in fabricating Co-SAs/NSC. For comparison, the samples with the same loading of the Co content were also prepared under the identical conditions without utilization of S- or N-species. As illustrated in Fig. S11 in the ESM, XRD pattern shows the characteristic peaks of Co nanoparticles. Futhermore, the mass-production of Co-SAs/NSC was also implemented (Fig. S12 in the ESM). No metallic Co signals appear in the XRD pattern of the scaled-up preparation of the Co-SAs/NSC, and ca. 713 mg of Co-SAs/NSC can be prepared under our experimental conditions (Fig. S13 in the ESM). The results futher demonstrate that strong interaction between Co centers and N, S atoms effectively prevents the agglomeration of high density Co atoms.

3.2 Electro-oxidation performance

MPS is one of the simplest aromatic thioethers, and corresponding oxidative product can be directly utilized as fine chemicals for pharmaceutical, plastics, and chemical industry [40, 41]. Herein, MPS was selected as a model molecule to evaluate the electro-oxidation activity of the Co-SAs/NSC in a mixed acidic electrolyte of 0.5 M CH_3COOH and 0.25 M K_2SO_4 (pH = 2.8). Figure 3(a)

gives the LSV curves in the presence and absence of MPS. The Co-SAs/NSC exhibits outstanding electro-oxidation activity in the presence of MPS, achieving a current density of 10 mA·cm^{-2} at a rather low potential of ~ 1.44 V vs. RHE. The potential is significantly reduced by 460 mV (from 1.90 to 1.44 V) in comparison with the absence of MPS. Furthermore, the corresponding charge transfer resistance of Co-SAs/NSC is also declined to 10 Ω after the injection of MPS, respectively (Fig. S14 in the ESM). The results indicate the low resistance of electron transport and fast mass transfer between Co sites and MPS. The ECSA of Co-SAs/NSC was also evaluated to further elucidate its high performance. Since C_{dl} is linearly proportional to ECSA [42], CV curves with scanning rates from 10 to 100 mV·s^{-1} were carried out at the non-Faradaic potential regions of 0.55–0.65 V vs. RHE to measure the value of C_{dl} (Fig. S15 in the ESM). The C_{dl} of Co-SAs/NSC is 11.4 mF·cm^{-2}, which is greater than that of the nanoparticle electrode (5.9 mF·cm^{-2}, Fig. S15 in the ESM). This result suggests that the Co-SAs/NSC intimates the existence of plentiful active sites, which endows the excellent electro-oxidation performance.

To further evaluate the electrocatalytic performance of Co-SAs/NSC, the oxidation product was collected and characterized by HPLC after electrolysis. Figure S16 in the ESM shows MPSO is the only electro-oxidation product for the conversion of MPs, suggesting a selective convesion process. Futhermore, the conversion rate of MPS over Co-SAs/NSC is ~ 99.7% at a low potential of 1.40 V vs. RHE during 4 h (Fig. 3(b)). The commercial Pt electrode requires a very high potential of 3.0 V to reach a similar conversion rate [21]. The results futher imply the extraordinary electrocatalytic activity of Co-SAs/NSC for the selective oxidation of MPS, which, meanwhile, is much superior to other state-of-the-art catalysts (Table S4 in the ESM) [22]. Moreover, the constant-potential electrolysis of MPS on Co-SAs/NSC was conducted at various potentials from 1.40 to 1.80 V vs. RHE. As shown in Fig. S17 in the ESM, high conversion rate of MPS with high selectivity toward MPSO maintains very well even upon increasing potential to 1.80 V vs. RHE, and FE can still reach 87.8% (Fig. 3(c)). Meanwhile, the reaction time is shortened to 0.5 h (Fig. S18 in the ESM). Particularly, no obviously decay of electrocatalytic performance occurs after proceeding 5 cycles (Fig. 3(d)), showing the robust stability of Co-SAs/NSC. The HAADF-STEM and the EDS mapping images of Co-SAs/NSC after the reaction (Figs. S19 and S20 in the ESM) show that the Co atoms still maintain the uniform distribution after the constant-potential electrolysis. Addtionally, the content of Co in the electrolyte solution was measured to evaluate the anticorrosion capacity of Co-SAs/NSC. As displayed in Fig. S21 in the ESM, no Co component was detected, indicating its remarkable durability for the acidic electrolyte.

3.3 Mechanism of electro-oxidation

To decode the underlying reaction process for electro-oxidation, identifying the role of Co SAs and tracking the source of active [O] species in MPSO are significantly necessary. Thus a series of controlled experiments were implemented. Firstly, the Co-NPs/NSC and the pure NSC as referenced electrocatalysts were prepared (Figs. S22 and S23 in the ESM) to investigate their electro-oxidation performance under the identical conditions. As shown in Fig. S24 in the ESM, relative to the pure NSC, the electrocatalytic activities of the Co-containing catalysts (Co-SAs/NSC and Co-NPs/NSC) are apparently enhanced, suggesting the Co component should be the active species in oxidation of MPS. Moverover, among three samples, Co-SAs/NSC shows the best electro-oxidation performacne than Co-NPs/NSC and bare NSC (Figs. S24 and S25 in the ESM). Both the current density and the conversion rate of MPS over Co-SAs/NSC obviously surpass those over Co-NPs/NSC (Fig. S24 in the ESM). These results imply that Co SAs might be the dominant active centers. Furthermore, owing to the fact that thiocyanate (SCN^-) represents a strong affinity with most metal ions, the Co SAs of Co-SAs/NSC can quickly bond with SCN^-. Thus the study of electrolyzing SCN^- over Co-SAs/NSC can evidence the active sites. As expected, the

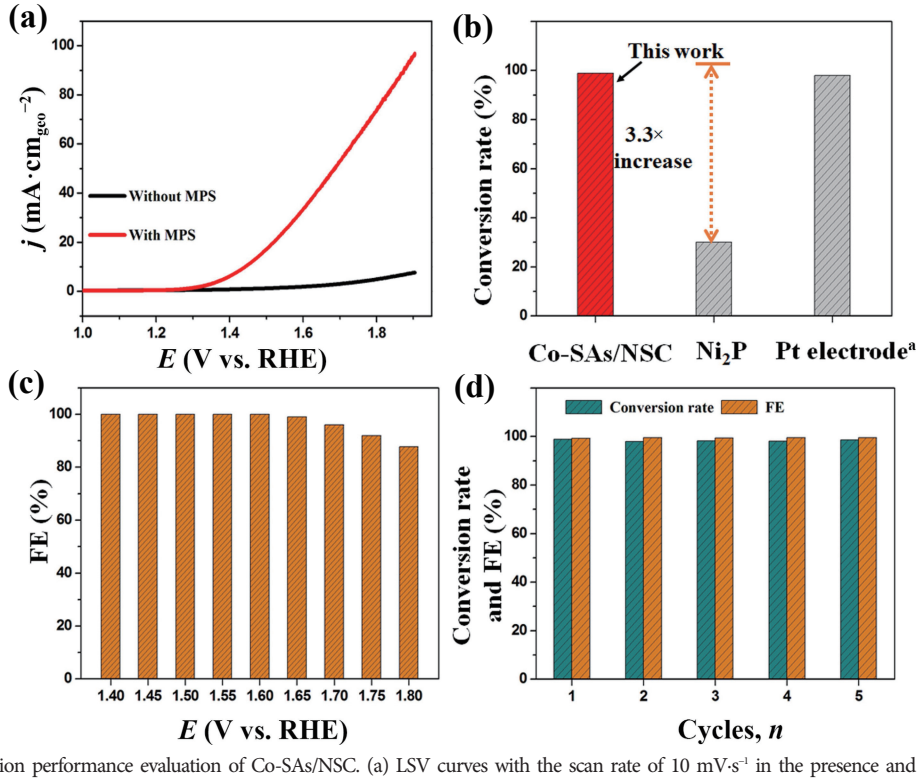

Figure 3 Electro-oxidation performance evaluation of Co-SAs/NSC. (a) LSV curves with the scan rate of 10 mV·s^{-1} in the presence and the absence of MPS. (b) Comparison of conversion rate of MPS over Co-SAs/NSC with other catalysts at 1.40 V vs. RHE (^{a}the potential for Pt electrode is at 3.0 V). (c) FE of MPSO at various potentials over Co-SAs/NSC. (d) Cyclic stability over Co-SAs/NSC at 1.40 V vs. RHE.

current intensity of Co-SAs/NSC is further enchanced when SCN^- ions (0.1 mmol) was introduced into the electrolysis system (Fig. 4(a)). The result demonstrates Co species is the active component in electro-oxidation of MPS, and the isolated Co SAs serve as the active centers. On the other hand, unraveling the evolution of Co SAs during electrocatalysis is also very important for understanding the reaction mechanism. Therefore, the glassy carbon electrode (GCE) modified by Co-SAs/NSC as working electrode was used to analyze the electrochemical behavior of Co SAs through the LSV curves. Figure 4(b) shows a disappearing oxidation peak of Co^{II}/Co^{III} at ca. 1.30 V vs. RHE after the addition of MPS. Meanwhile, the Co XPS spectra after 1 and 4 h reaction exhibit that the binding energy position of Co has no obvious change in comparison with the fresh sample (Fig. S26 in the ESM). These facts imply that the electro-oxidation of MPS is dominated by the *in situ* formed Co^{II}/Co^{III} species in Co-SAs/NSC.

Furthermore, tracking the transferred trace of active [O] in product is vital to unveil the electro-oxidation mechanism. Thus the role of oxygen and water as a possible [O] source in electro-oxidation was investigated, respectively. As shown in Fig. 4(c), a weak current intensity was observed in O_2-saturated acetonitrile electrolyte, suggesting Co-SAs/NSC shows the sluggish response for the electro-oxidation of MPS. While the current intensity increased rapidly after the addition of a little amount of H_2O into the above soultion. Moreover, similiar current intensity can also be realized in Ar-saturated acetonitrile with H_2O in the absence of O_2 (Fig. 4(c)), implying H_2O molecule might be the source of [O] for MPSO. To further confirm this proposal, the gas product at Co-SAs/NSC anode was collected and determined by the GC. As illustrated in Fig. S27 in the ESM, an obvious signal of H_2 can be clearly observed, produced from H_2O water splitting at Co-SAs/NSC anode. This result adequately confirms that H_2O as a feedstock was participated in the electro-oxidation. Therefore, based on the above comprehensive analysis, we reasonably speculate the electro-oxidation process over Co-SAs/NSC: Firstly, in the presence of MPS, the Co SAs of Co-SAs/NSC were converted into high oxidation state with the assistance of applied voltage, then MPS was quickly transformed by the oxidized Co SAs using H_2O as oxygen source into MPSO, meanwhile the Co SAs were restored to the initial oxidation state in the process. So that the oxidation peak of Co cannot be detected in the corresponding LSV curves and the Co XPS spectra after electro-oxidation in the presence of MPS (Fig. 4(d) and Fig. S28 in the ESM).

According to the above mechanism analysis, DFT calculation was performed to futher gain insight into the role of Co SAs in electro-oxidation. Figure 4(e), and Figs. S29 and S30 in the ESM display the adsorption free energies and the adsorption geometry of MPS on the optimized Co-SAs/NSC and the (101) face of Co NPs, respectively. It was clearly observed that MPS was adsorbed onto Co SAs through S atoms, forming a twisted adsorption structure with adsorption energy of ca. −0.17 eV. For comparison, due to the π–electron interaction between phenyl group and the Co NPs, the whole skeleton of MPS was tightly fixed on the surface of Co NPs, leading to a much higher adsorption energy of ca. −0.43 eV. This result shows isolated Co centers can accurately bond to the reaction sites of the substrate molecules, and the nanoscale catalysts show indiscriminate adsorption with substrate groups (Fig. S29 in the ESM). Subsequently, the excited MPS adsorbed on the surface of catalysts was converted to MPSO through bonding with [O] species from H_2O, in which the formation energies of [O] with Co SAs and Co NPs are ca. 0.70 and 0.46 eV, respectively. This larger energy of MPSO with Co SAs means MPSO cannot be stably adsorbed on the surface of Co SAs, which promotes the desorption of the product. As a result, the desorption energies of MPSO over Co SAs and Co NPs are ca. 0.65 and 1.17 eV (Fig. 4(e) and Fig. S29(b) in the ESM), respectively. The result reveals that the isolated metal structure is in favor of releasing the catalytic products, which might be one of the reasons that SAs catalyts possesses higher catalytic performance than their NPs in most heterogeneous reactions. Additionally, we found that the Co SAs can precisely interact with the S-group of MPS after analysis of the adsorption model between Co-SAs/NSC and MPS. Thus electro-oxidation of MPS derivatives containing diffent active groups (such as $–NH_2$, –OH, and –CHO) was also carried out over Co-SAs/NSC to investigate

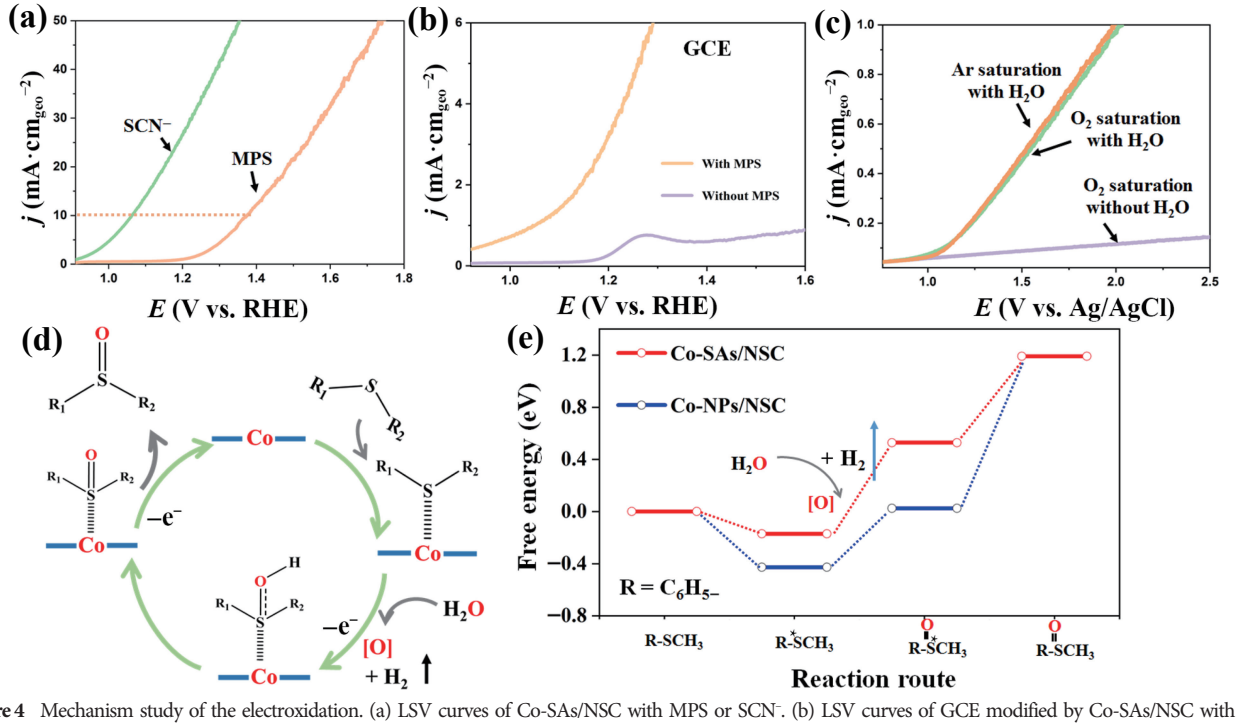

Figure 4 Mechanism study of the electroxidation. (a) LSV curves of Co-SAs/NSC with MPS or SCN^-. (b) LSV curves of GCE modified by Co-SAs/NSC with and without MPS. (c) LSV curves of Co-SAs/NSC with MPS and H_2O in Ar or O_2-saturated acetonitrile electrolyte. (d) Possible reaction mechanism of MPS to MPSO over Co-SAs/NSC. (e) Energy profiles of the conversion of MPS to MPSO over Co-SAs/NSC and Co-NPs/NSC.

the substrate universality. As shown in Fig. 5 and Fig. S31 in the ESM, these substrates were efficiently converted into corresponding sulfoxide products, demonstrating that the obtained Co SAs have excellent selectivity and universality.

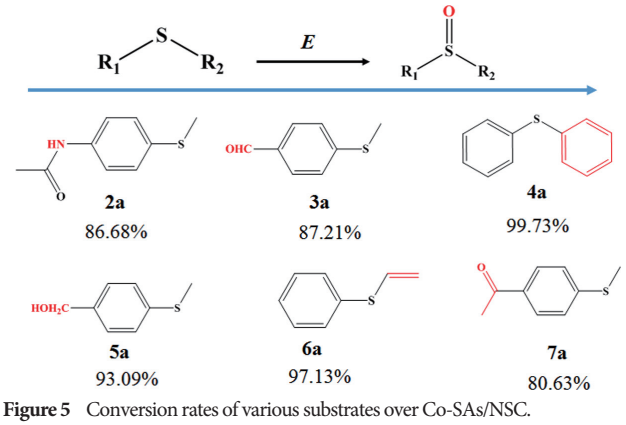

Figure 5 Conversion rates of various substrates over Co-SAs/NSC.

4 Conclusions

In summary, we have fabricated N,S co-doped carbon to successfully anchor high-density single atoms Co (Co-SAs/NSC) with the loading amount of 10 wt.%. The N,S co-doped carbon structure results in a unique coordination geometry of Co-S_2N_4 for Co SAs, delivering excellent electrocatalytic activity and the robust stability for electro-oxidation of various thioethers in acid electrolyte. As a result, the conversion rate of methyl phenyl sulfide can reach up to 99.7%, accompanying with 100% selectivity and 100% FE for methylphenyl sulfoxide, over Co-SAs/NSC at the low voltage of 1.40 V vs. RHE. This performance is much higher than that of Pt electrode and other reported catalysts at the same voltage. A series of controlled experiments and DFT calculation reveal that the active centers of isolated Co SAs promote the desorption of products, exhibiting extraordinary electro-oxidation performance. This work represents a significant advancement in developing high density metal single atom electrocatalysts and opens up new opportunities for the resourceful use of sulfur-containing pollutants.

Acknowledgements

This work was supported by the National Natural Science Foundation of China (Nos. 22275139, 21773288, and U1932119), the National Key Basic Research Program of China (No. 2017YFA040340), and the Natural Science Foundation of Tianjin City of China (No. 18JCJQJC47700).

Electronic Supplementary Material: Supplementary material (SEM, XRD, Raman spectrum, HRTEM, HAADF-STEM images, DFT structure, and performance evaluations) is available in the online version of this article at https://doi.org/10.1007/s12274-023-5381-z.

References

[1] Hai, X.; Xi, S. B.; Mitchell, S.; Harrath, K.; Xu, H. M.; Akl, D. F.; Kong, D. B.; Li, J.; Li, Z. J.; Sun, T. et al. Scalable two-step annealing method for preparing ultra-high-density single-atom catalyst libraries. *Nat. Nanotechnol.* **2022**, *17*, 174–181.

[2] Zhou, Y. Z.; Tao, X. F.; Chen, G. B.; Lu, R. H.; Wang, D.; Chen, M. X.; Jin, E. Q.; Yang, J.; Liang, H. W.; Zhao, Y. et al. Multilayer stabilization for fabricating high-loading single-atom catalysts. *Nat. Commun.* **2020**, *11*, 5892.

[3] Xiong, Y.; Sun, W. M.; Han, Y. H.; Xin, P. Y.; Zheng, X. S.; Yan, W. S.; Dong, J. C.; Zhang, J.; Wang, D. S.; Li, Y. D. Cobalt single atom site catalysts with ultrahigh metal loading for enhanced aerobic oxidation of ethylbenzene. *Nano Res.* **2021**, *14*, 2418–2423.

[4] Zhuang, Z. C.; Kang, Q.; Wang, D. S.; Li, Y. D. Single-atom catalysis enables long-life, high-energy lithium-sulfur batteries. *Nano Res.* **2020**, *13*, 1856–1866.

[5] Zhang, J. W.; Zeng, G. M.; Chen, L. L.; Lai, W. C.; Yuan, Y. L.; Lu, Y. F.; Ma, C.; Zhang, W. H.; Huang, H. W. Tuning the reaction path of CO_2 electroreduction reaction on indium single-atom catalyst: Insights into the active sites. *Nano Res.* **2022**, *15*, 4014–4022.

[6] Li, X. Y.; Rong, H. P.; Zhang, J. T.; Wang, D. S.; Li, Y. D. Modulating the local coordination environment of single-atom catalysts for enhanced catalytic performance. *Nano Res.* **2020**, *13*, 1842–1855.

[7] Pan, Y.; Ma, X. L.; Wang, M. M.; Yang, X.; Liu, S. J.; Chen, H. C.; Zhuang, Z. W.; Zhang, Y. H.; Cheong, W. C.; Zhang, C. et al. Construction of N,P co-doped carbon frames anchored with Fe single atoms and Fe_2P nanoparticles as a robust coupling catalyst for electrocatalytic oxygen reduction. *Adv. Mater.* **2022**, *34*, 2203621.

[8] Li, Z. J.; Leng, L. P.; Lu, X. W.; Zhang, M. Y.; Xu, Q.; Horton, J. H.; Zhu. J. F. Single palladium atoms stabilized by β-FeOOH nanorod with superior performance for selective hydrogenation of cinnamaldehyde. *Nano Res.* **2022**, *15*, 3114–3121.

[9] Ren, Y. J.; Tang, Y.; Zhang, L. L.; Liu, X. Y.; Li, L.; Miao, S.; Su, D. S.; Wang, A. Q.; Li, J.; Zhang, T. Unraveling the coordination structure–performance relationship in Pt_1/Fe_2O_3 single-atom catalyst. *Nat. Commun.* **2019**, *10*, 4500.

[10] Zhang, J.; Wu, X.; Cheong, W. C.; Chen, W. X.; Lin, R.; Li, J.; Zheng, L. R.; Yan, W. S.; Gu, L.; Chen, C. et al. Cation vacancy stabilization of single-atomic-site $Pt_1/Ni(OH)_x$ catalyst for diboration of alkynes and alkenes. *Nat. Commun.* **2018**, *9*, 1002.

[11] Reier, T.; Nong, H. N.; Teschner, D.; Schlögl, R.; Strasser, P. Electrocatalytic oxygen evolution reaction in acidic environments—Reaction mechanisms and catalysts. *Adv. Energy Mater.* **2017**, *7*, 1601275.

[12] Xiang, K.; Wu, D.; Deng, X. H.; Li, M.; Chen, S. Y.; Hao, P. P.; Guo, X. F.; Luo, J. L.; Fu, X. Z. Boosting H_2 generation coupled with selective oxidation of methanol into value-added chemical over cobalt hydroxide@hydroxysulfide nanosheets electrocatalysts. *Adv. Funct. Mater.* **2020**, *30*, 1909610.

[13] Li, N. N.; Zhu, C.; Zhang, J. W.; Jing, H. Y.; Hu, J. W.; Hao, C.; Shi, Y. T. Single-atom-catalyst with abundant Co-S_4 sites for use as a counter electrode in photovoltaics. *Chem. Commun.* **2021**, *57*, 5302–5305.

[14] Cui, T. T.; Ma, L. N.; Wang, S. B.; Ye, C. L.; Liang, X.; Zhang, Z. D.; Meng, G.; Zheng, L. R.; Hu, H. S.; Zhang, J. W. et al. Atomically dispersed Pt-N_3C_1 sites enabling efficient and selective electrocatalytic C–C bond cleavage in lignin models under ambient conditions. *J. Am. Chem. Soc.* **2021**, *143*, 9429–9439.

[15] Wang, T. H.; Tao, L.; Zhu, X. R.; Chen, C.; Chen, W.; Du, S. Q.; Zhou, Y. Y.; Zhou, B.; Wang, D. D.; Xie, C. et al. Combined anodic and cathodic hydrogen production from aldehyde oxidation and hydrogen evolution reaction. *Nat. Catal.* **2021**, *5*, 66–73.

[16] Zhang, Y. Q.; Zhou, B.; Wei, Z. X.; Zhou, W.; Wang, D. D.; Tian, J.; Wang, T. H.; Zhao, S. L.; Liu, J. L.; Tao, L. et al. Coupling glucose-assisted Cu(I)/Cu(II) redox with electrochemical hydrogen production. *Adv. Mater.* **2021**, *33*, 2104791.

[17] Yang, G. C.; Jiao, Y. Q.; Yan, H. J.; Xie, Y.; Tian, C. G.; Wu, A. P.; Wang, Y.; Fu, H. G. Unraveling the mechanism for paired electrocatalysis of organics with water as a feedstock. *Nat. Commun.* **2022**, *13*, 3125.

[18] Zheng, J.; Chen, X. L.; Zhong, X.; Li, S. Q.; Liu, T. Z.; Zhuang, G. L.; Li, X. N.; Deng, S. W.; Mei, D. H.; Wang, J. G. Hierarchical porous NC@CuCo nitride nanosheet networks: Highly efficient bifunctional electrocatalyst for overall water splitting and selective electrooxidation of benzyl alcohol. *Adv. Funct. Mater.* **2017**, *27*, 1704169.

[19] Zhu, P.; Shen, Y. L.; Dai, L. X.; Yu, Q. Y.; Zhang, Z. M.; An, C. H. Accelerating anode reaction with electro-oxidation of alcohols over Ru nanoparticles to reduce the potential for water splitting. *ACS Appl. Mater. Interfaces* **2022**, *14*, 1452–1459.

[20] Laudadio, G.; Straathof, N. J. W.; Lanting, M. D.; Knoops, B.; Hessel, V.; Noël, T. An environmentally benign and selective electrochemical oxidation of sulfides and thiols in a continuous-flow microreactor. *Green Chem.* **2017**, *19*, 4061–4066.

[21] Liu, S. W.; Chen, B. C.; Yang, Y.; Yang, Y. H.; Chen, Q. J.; Zeng, X. J.; Xu, B. Electrochemical oxidations of thioethers: Modulation of oxidation potential using a hydrogen bonding network. *Electrochem. Commun.* **2019**, *109*, 106583.

[22] Han, S. Y.; Wang, C. H.; Shi, Y. M.; Liu, C. B.; Yu, Y. F.; Lu, S. Y.; Zhang, B. Membrane-free selective oxidation of thioethers with water over a nickel phosphide nanocube electrode. *Cell Rep. Phys. Sci.* **2021**, *2*, 100462.

[23] Wang, X. Y.; Chen, L. J.; Chong, S. Y.; Little, M. A.; Wu, Y. Z.; Zhu, W. H.; Clowes, R.; Yan, Y.; Zwijnenburg, M. A.; Sprick, R. S. et al. Sulfone-containing covalent organic frameworks for photocatalytic hydrogen evolution from water. *Nat. Chem.* **2018**, *10*, 1180–1189.

[24] Kaiser, D.; Klose, I.; Oost, R.; Neuhaus, J.; Maulide, N. Bond-forming and -breaking reactions at sulfur(IV): Sulfoxides, sulfonium salts, sulfur ylides, and sulfinate salts. *Chem. Rev.* **2019**, *119*, 8701–8780.

[25] Clark, S. J.; Segall, M. D.; Pickard, C. J.; Hasnip, P. J.; Probert, M. I. J.; Refson, K.; Payne, M. C. First principles methods using CASTEP. *Z. Kristallogr.—Cryst. Mater.* **2005**, *220*, 567–570.

[26] Hohenberg, P.; Kohn, W. Inhomogeneous electron gas. *Phys. Rev.* **1964**, *136*, B864–B871.

[27] Perdew, J. P.; Ruzsinszky, A.; Csonka, G. I.; Vydrov, O. A.; Scuseria, G. E.; Constantin, L. A.; Zhou, X. L.; Burke, K. Restoring the density-gradient expansion for exchange in solids and surfaces. *Phys. Rev. Lett.* **2008**, *100*, 136406.

[28] Head, J. D.; Zerner, M. C. A Broyden–Fletcher–Goldfarb–Shanno optimization procedure for molecular geometries. *Chem. Phys. Lett.* **1985**, *122*, 264–270.

[29] Vanderbilt, D. Soft self-consistent pseudopotentials in a generalized eigenvalue formalism. *Phys. Rev. B* **1990**, *41*, 7892–7895.

[30] Liang, C.; Chen, Y.; Wu, M.; Wang, K.; Zhang, W. K.; Gan, Y. P.; Huang, H.; Chen, J.; Xia, Y.; Zhang, J. et al. Green synthesis of graphite from CO_2 without graphitization process of amorphous carbon. *Nat. Commun.* **2021**, *12*, 119.

[31] Boppella, R.; Austeria P, M.; Kim, Y.; Kim, E.; Song, I.; Eom, Y.; Kumar, D. P.; Balamurugan, M.; Sim, E.; Kim, D. H. et al. Pyrrolic N-stabilized monovalent Ni single-atom electrocatalyst for efficient CO_2 reduction: Identifying the role of pyrrolic-N and synergistic electrocatalysis. *Adv. Funct. Mater.* **2022**, *32*, 2202351.

[32] Shen, R. A.; Chen, W. X.; Peng, Q.; Lu, S. Q.; Zheng, L. R.; Cao, X.; Wang, Y.; Zhu, W.; Zhang, J. T.; Zhuang, Z. B. et al. High-concentration single atomic Pt sites on hollow CuS_x for selective O_2 reduction to H_2O_2 in acid solution. *Chem* **2019**, *5*, 2099–2110.

[33] Min, Y.; Zhou, X.; Chen, J. J.; Chen, W. X.; Zhou, F. Y.; Wang, Z. Y.; Yang, J.; Xiong, C.; Wang, Y.; Li, F. T. et al. Integrating single-cobalt-site and electric field of boron nitride in dechlorination electrocatalysts by bioinspired design. *Nat. Commun.* **2021**, *12*, 303.

[34] Li, J. C.; Meng, Y.; Zhang, L. L.; Li, G. Z.; Shi, Z. C.; Hou, P. X.; Liu, C.; Cheng, H. M.; Shao, M. H. Dual-phasic carbon with Co single atoms and nanoparticles as a bifunctional oxygen electrocatalyst for rechargeable Zn-air batteries. *Adv. Funct. Mater.* **2021**, *31*, 2103360.

[35] Han, X. P.; Ling, X. F.; Wang, Y.; Ma, T. Y.; Zhong, C.; Hu, W. B.; Deng, Y. D. Generation of nanoparticle, atomic-cluster, and single-atom cobalt catalysts from zeolitic imidazole frameworks by spatial isolation and their use in zinc-air batteries. *Angew. Chem., Int. Ed.* **2019**, *58*, 5359–5364.

[36] Yuan, S.; Pu, Z. H.; Zhou, H.; Yu, J.; Amiinu, I. S.; Zhu, J. W.; Liang, Q. R.; Yang, J. L.; He, D. P.; Hu, Z. Y. et al. A universal synthesis strategy for single atom dispersed cobalt/metal clusters heterostructure boosting hydrogen evolution catalysis at all pH values. *Nano Energy* **2019**, *59*, 472–480.

[37] Li, N.; Song, X. Z.; Wang, L.; Geng, X. L.; Wang, H.; Tang, H. Y.; Bian, Z. Y. Single-atom cobalt catalysts for electrocatalytic hydrodechlorination and oxygen reduction reaction for the degradation of chlorinated organic compounds. *ACS Appl. Mater. Interfaces* **2020**, *12*, 24019–24029.

[38] Li, Y. L.; Jia, B. M.; Fan, Y. Z.; Zhu, K. L.; Li, G. Q.; Su, C. Y. Bimetallic zeolitic imidazolite framework derived carbon nanotubes embedded with Co nanoparticles for efficient bifunctional oxygen electrocatalyst. *Adv. Energy Mater.* **2018**, *8*, 1702048.

[39] Wang, Y.; Li, J. L.; Shi, W. X.; Zhang, Z. M.; Guo, S.; Si, R.; Liu, M.; Zhou, H. C.; Yao, S.; An, C. H. et al. Unveiling single atom nucleation for isolating ultrafine fcc Ru nanoclusters with outstanding dehydrogenation activity. *Adv. Energy Mater.* **2020**, *10*, 2002138.

[40] Ilardi, E. A.; Vitaku, E.; Njardarson, J. T. Data-mining for sulfur and fluorine: An evaluation of pharmaceuticals to reveal opportunities for drug design and discovery. *J. Med. Chem.* **2014**, *57*, 2832–2842.

[41] Wang, N. Z.; Saidhareddy, P.; Jiang, X. F. Construction of sulfur-containing moieties in the total synthesis of natural products. *Nat. Prod. Rep.* **2020**, *37*, 246–275.

[42] Voiry, D.; Chhowalla, M.; Gogotsi, Y.; Kotov, N. A.; Li, Y.; Penner, R. M.; Schaak, R. E.; Weiss, P. S. Best practices for reporting electrocatalytic performance of nanomaterials. *ACS Nano* **2018**, *12*, 9635–9638.